Micron 109 (2018) 58–70

Contents lists available at ScienceDirect

Micron

journal homepage: www.elsevier.com/locate/micron

Three-dimensional geometrical and topological characteristics of grains in conventional and grain boundary engineered 316L stainless steel

Tingguang Liu[a,c], Shuang Xia[a,b,*], Bangxin Zhou[a,b], Qin Bai[a], Gregory S. Rohrer[d]

[a] Institute of Materials, School of Materials Science and Engineering, Shanghai University, Shanghai 200072, China
[b] State Key Laboratory of Advanced Special Steel, Shanghai University, Shanghai 200072, China
[c] National Center for Materials Service Safety, University of Science and Technology Beijing, Beijing 100083, China
[d] Department of Materials Science and Engineering, Carnegie Mellon University, Pittsburgh, PA 15213, USA

ARTICLE INFO

Keywords:
316L stainless steel
3D EBSD
Grain boundary engineering
Grain
Grain boundary

ABSTRACT

The three-dimensional microstructures of a conventional 316L stainless steel and the same material after grain boundary (GB) engineering have been measured by serial sectioning coupled with electron backscatter diffraction mapping. While it is well known that GB engineered materials are differentiated from conventional materials because of the proportion of coincidence site lattice boundaries, the size of their twin-related domains, and their reduced random boundary connectivity, this work provides a quantitative comparison of the geometrical and topological characteristics of grains in 316L stainless steel before and after GB engineering. Specifically, the numbers of grain faces, triple lines, and quadruple unions per grain have been measured and compared. In addition, the distributions of grain sizes, surface areas, and grain boundary areas have been measured and compared. The results show that, in many ways, the three-dimensional geometrical and topological characteristics of the grains in the GB engineered and conventional materials are similar. In both materials, the distributions of the geometrical parameters are well represented by a log-normal distribution. Comparatively, the GB engineered microstructure has grains that, on average, have both fewer faces and higher (specific) surface areas that deviate more from an ideal equiaxed shape, but there are several eccentric or non-compact shaped grains that have a huge number of faces and extremely large surface area in the GB engineered material. All of these characteristics are likely to be a result of the increased number of twins in the GB engineered microstructure. These eccentric grains would have a positive influence on increasing the resistance to intergranular degradation.

1. Introduction

Since the early 1980s, a promising method, known as 'grain boundary engineering' (GBE) (Kumar et al., 2000; Liu et al., 2014b; Michiuchi et al., 2006; Randle, 2004; Tokita et al., 2017; Watanabe, 1984), has been used to improve grain boundary (GB) related properties of some not only structural but also functional materials (Watanabe, 2011), particularly face-centered-cubic (FCC) materials with low stacking fault energy. Among these properties are intergranular corrosion (Hu et al., 2011; Kobayashi et al., 2016; Xia et al., 2011), intergranular stress corrosion cracking (Gertsman and Bruemmer, 2001; Palumbo et al., 1991; Tan et al., 2013; Telang et al., 2016; West and Was, 2009), and creep (Alexandreanu et al., 2003; Alexandreanu and Was, 2006). The improved properties are thought to emerge because the GB engineering process increases the concentration of coincidence site lattice (CSL) boundaries with high coincidence. Some low-Σ CSL boundaries (where $\Sigma \leq 29$ and measures the inverse coincidence) have shown better performance than random boundaries in FCC materials (Hu et al., 2011; Kobayashi et al., 2016; Palumbo et al., 1991; Tan et al., 2013; Telang et al., 2016; Xia et al., 2011). Numerous studies (Cao et al., 2017; Kumar et al., 2000; Liu et al., 2014a, 2013; Michiuchi et al., 2006; Randle, 2004; Xia et al., 2008) have investigated the GB character distribution (GBCD) of materials before and after GB engineering, finding that the prominent characteristics of GB engineered microstructures include a high proportion of low-Σ CSL boundaries, large twin-related domains, and a disrupted random boundary network. However, these studies have mostly been based on comparisons of two-dimensional (2D) microstructural data from materials before and after GB engineering. One recent study has compared twin related domains in the three-dimensional (3D) microstructures of conventional and GB engineered copper (Lind et al., 2016). However, a comparison of the geometrical characteristics of

* Corresponding author at: P O Box 269, 149 Yanchang Road, Shanghai, 200072, China. Tel.: +86-18019322802.
E-mail addresses: xs@shu.edu.cn, xiashuang14@sohu.com (S. Xia).

https://doi.org/10.1016/j.micron.2018.04.002
Received 7 February 2018; Received in revised form 8 April 2018; Accepted 8 April 2018
Available online 10 April 2018
0968-4328/

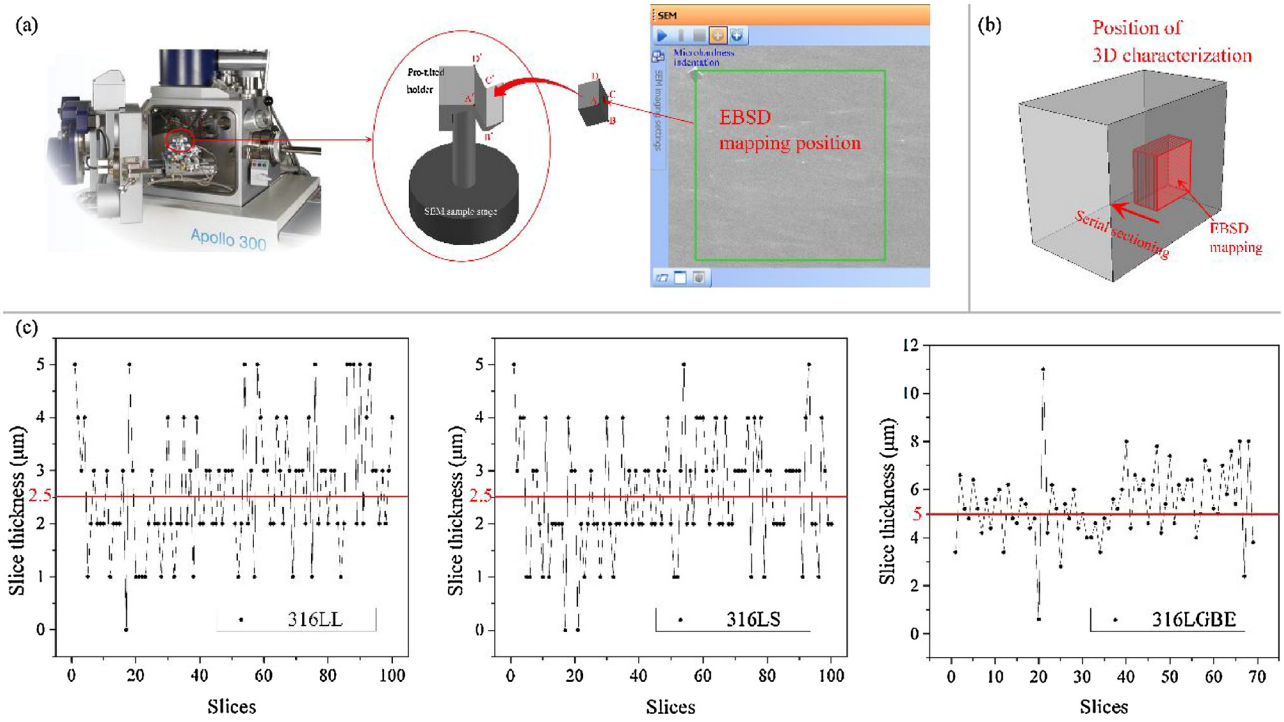

Fig. 1. (a) Schematic drawings of the positioning method used for the EBSD data collection, (b) the serial-sectioning used for 3D characterization, and (c) the slice thickness distributions of the three samples.

grains in conventional and GB engineered microstructures has not yet been extensively reported. In the current paper, we compare 3D data from a 316L stainless steel that has been GB engineered with conventional material that has not been GB engineered. The 3D data allows us to compare the microstructural parameters that cannot be derived from 2D observations including grain shapes and the numbers of grain faces, triple lines, and quadruple points. It is well-known grain boundaries have great contribution to the behavior of materials. Furthermore, the properties of materials are closely correlated with the triple junctions and quadruple junctions, such as coordination deformation between neighboring grains during deformation, and intergranular damage route at triple lines and quadruple points (Hu et al., 2011).

The most common methods of obtaining 3D orientation maps of microstructures are serial sectioning coupled with electron backscatter diffraction (EBSD) mapping (Kelly et al., 2016; Lewis et al., 2006; Rowenhorst et al., 2010; Saylor et al., 2002; Uchic et al., 2006) and X-ray diffraction techniques including high energy diffraction microscopy (HEDM) (Hefferan et al., 2012; Lin et al., 2015), differential contrast tomography (DCT) (King et al., 2008), differential aperture x-ray microscopy (DAXM) (Larson et al., 2002). Serial sectioning can be accomplished either with a focused ion beam (FIB) (Kelly et al., 2016; Saylor et al., 2002; Uchic et al., 2006) or by subtractive polishing (Alkemper and Voorhees, 2001; Lewis et al., 2006; Rowenhorst et al., 2010; Spowart, 2006). The FIB method is attractive because the process can be automated so that in a few days, a large number of grains can be characterized. However, the disadvantage is that the field of view is rather small. Even using newly available Xe-ion plasma FIBs, it is not currently possible to examine volumes with lateral dimensions much greater than 200 μm (Kelly et al., 2016). While serial sectioning by subtractive polishing is more difficult to implement, the field of view is not restricted and this makes it possible to study materials with larger grain sizes that are used in structural applications (Rowenhorst et al., 2010).

In 3D microstructures, one can identify four geometrical and topological characteristics of grains that cannot be completely quantified in 2D microstructures: the grain shape, the grain boundaries (faces), the grain edges (triple lines between three grains), and the grain vertices (quadruple points between four grains) (Bhandari et al., 2007; Groeber et al., 2008; Ullah et al., 2014). Furthermore, the connectivity of grain boundaries, including chains of twins that are important in GB engineered materials (Rohrer and Miller, 2010; Xia et al., 2009), can be identified from 3D data, but they cannot be determined from 2D data. In the current study, we will quantify and compare the geometrical and topological characteristics of the grains in GB engineered and conventional 316L stainless steels.

Past 3D studies of polycrystalline materials have found that the grain size distribution is reasonably well approximated by a log-normal distribution (Rowenhorst et al., 2010; Ullah et al., 2014; Zhang et al., 2004). Past measurements of the mean number of faces per grain have yielded 11.8 for β-brass (Hull, 1988), 12.1 for α-iron (Zhang et al., 2004), 12.8 for pure iron (Ullah et al., 2014), 12.9 for a Ni superalloy (Groeber et al., 2008), 13.7 for β-titanium (Rowenhorst et al., 2010), and 14.2 for α-titanium (Kelly et al., 2016). Therefore, to a good approximation, one can say that, on average, there are between 12 and 14 faces per grain. It has also been shown that the number of faces is positively correlated to the grain size (Hull, 1988; Kelly et al., 2016; Rowenhorst et al., 2010). In past work, features such as triple lines and quadruple points have not been given as much attention (Hardy and Field, 2016; Li et al., 2014; Ullah et al., 2014).

While the high proportion of twin-related boundaries is well known for the GB engineered materials, changes in the grain geometrical characteristics of grains before and after GB engineering are also of interest but have not been reported. The main goal of this paper is to quantify and compare the grain sizes, grain surface areas, and grain face areas within the microstructures of conventional and GB engineered 316L stainless steels. We will also examine the numbers of grain faces, triple lines and quadruple points per grain, and correlations with grain sizes. The 3D twin boundaries and GB networks of the 316L stainless steels before and after GB engineering have been reported in other papers (Liu et al., 2017).

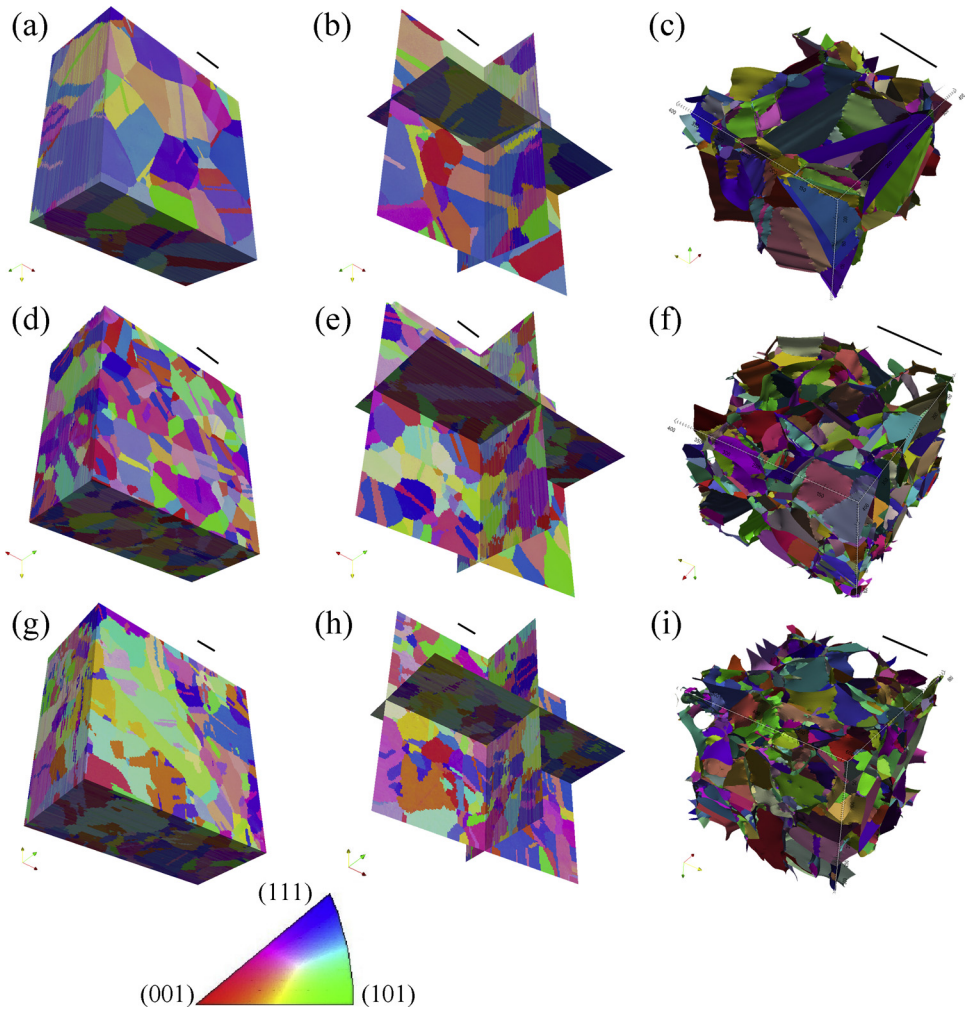

Fig. 2. Visualizations of the 3D-EBSD maps of the three samples: 316LL (a, b, c), 316LS (d, e, f) and 316LGBE (g, h, i). Maps a, b, d, e, g and h are colored according to the inverse pole figure (IPF) of direction Z, and maps c, f and i show the GB networks which are colored according to the GB misorientations. The length of the scale bar in each of the images are 100 μm.

2. Materials and methods

2.1. Materials

Three samples, designated as 316LL, 316LS, and 316LGBE, were produced from a conventional, commercially available 316L stainless steel product. The starting 316L material was rolled to a 50% reduction in thickness at 1000 °C and then water quenched. Subsequently, it was cut into three parts using an electro discharge machining. Two parts were recrystallized with a 150 min anneal at 1050 °C (316LL with a mean grain diameter of 49.8 μm measured in a 2D EBSD map) and a 30 min anneal at 1000 °C (316LS with a mean grain diameter of 31.6 μm measured in a 2D EBSD map), respectively. The grain size of 316LL is larger than that of 316LS due to grain growth during the longer annealing. The third part was annealed at 1000 °C for 30 min followed by water quenching. Next, it was warm rolled to a 5% reduction of thickness at a starting temperature 400 °C and then water quenched. In the final step, it was annealed at 1100 °C for 60 min for full recrystallization and then water quenched (316LGBE with a mean grain diameter of 43.2 μm measured in a 2D EBSD map). The process of warm-rolling with low-strain deformation, combined with high temperature annealing, was intended to create a high fractional population of twin-boundaries, as in a previously described GB engineering process (Liu et al., 2014a, 2013; Xia et al., 2008).

2.2. 3D EBSD mapping

Serial-sectioning and EBSD mapping (Lewis et al., 2006; Lin et al., 2010; Rowenhorst et al., 2010; Zhang et al., 2004) were used to obtain the 3D microstructure data with the following workflow.

(1) Serial-sectioning. To obtain a certain thickness reduction, the samples were manually mechanically-polished under a fixed load and for fixed times. The target thickness reduction was 2.5 μm for 316LL and 316LS, and it was 5 μm for 316LGBE. A suspension of sol-gel produced alumina (0.05 μm) was used during the polishing in order to produce a good surface for EBSD mapping.
(2) Thickness measurement. A micrometer with a precision of 1 μm was used to measure the reduction of thickness after each polishing step.
(3) Positioning and alignment. Micro-hardness indents were used to mark the region of interest for EBSD mapping.
(4) EBSD mapping. The crystal orientations on the surface after each polishing step were measured by EBSD using an HKL/Channel 5 EBSD system that was integrated with a CamScan Apollo 300 field emission scanning electron microscope (SEM). The EBSD mapping field of view was 600 μm × 600 μm for samples 316LL and 316LS, and the step size was 2.5 μm. For 316LGBE, the mapping field of view was 800 μm × 800 μm with a step size of 5 μm.

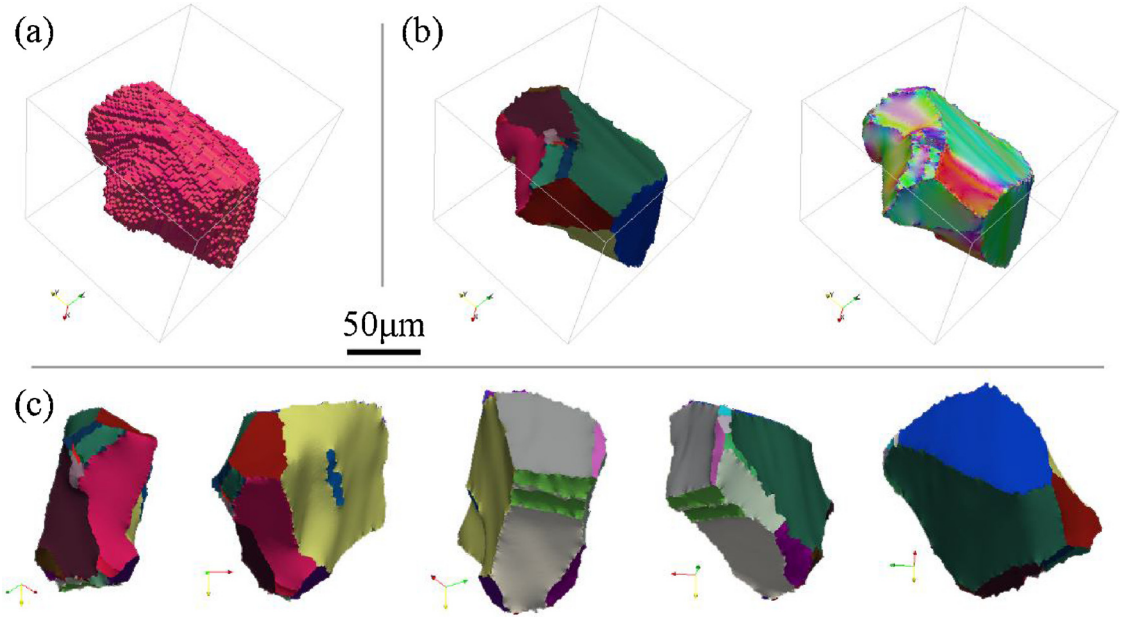

Fig. 3. The 3D visualizations of a typical grain from specimen 316LL: (a) the raw data illustrating that the grain is composed of voxels. (b) The grain after smoothing: the left hand figure is colored according to the grain boundary misorientations, and the right hand figure is colored according to the local boundary orientation in the crystal reference frame using the IPF coloring code (as in Fig. 2). (c) Visualizations of the grain in different projections.

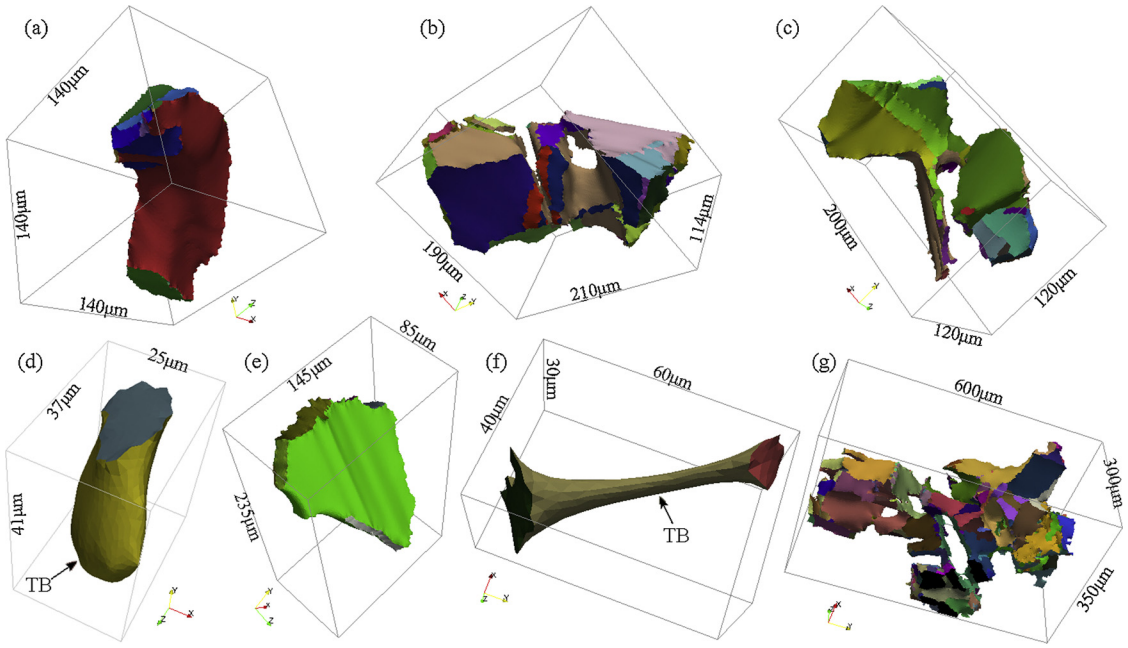

Fig. 4. 3D visualizations of several typical grains. The equivalent spherical diameters of these grains are 101.8 μm (a), 126.8 μm (b), 93.5 μm (c), 31.2 μm (d), 88.8 μm (e), 31.6 μm (f) and 249.3 μm (g), respectively. Grains a, b, c and e come from 316LS; grain d comes from 316LL; grains f and g come from 316LGBE.

The four steps listed above were repeated on the three samples, as shown schematically in Fig. 1(a and b). A total of 101 parallel sections were mapped for samples 316LL and 316LS, and the average thicknesses per slice were 2.65 μm and 2.55 μm, respectively. For 316LGBE, 70 parallel sections were mapped, and the average thickness per slice was 5.39 μm. Fig. 1c shows the slice thickness distributions of the samples. The volumes of the three reconstructed 3D-EBSD microstructures were 600 μm × 600 μm × 267.6 μm (316LL), 600 μm × 600 μm × 257.5 μm (316LS), and 800 μm × 800 μm × 377.3 μm (316LGBE). The measured twin boundary length fractions in the 2D EBSD maps were 48.9% (316LL), 51.7% (316LS) and 65.4% (316LGBE) using Brandon criterion (Brandon, 1966). These measurements depict that, the GB engineering process increased the twin boundary length fraction in 316L.

2.3. Post-processing of 3D-EBSD data

Dream.3D v4.2.5004 (Groeber and Jackson, 2014) was used to reconstruct the parallel layers of 2D EBSD data into 3D microstructures; ParaView v4.3.1 (Ayachit, 2015) was used to visualize the microstructures. Dream.3D was also used to quantify the grain sizes, grain shape parameters, grain orientations, and the number of nearest neighbor grains. The Dream.3D pipelines used in this work are listed in

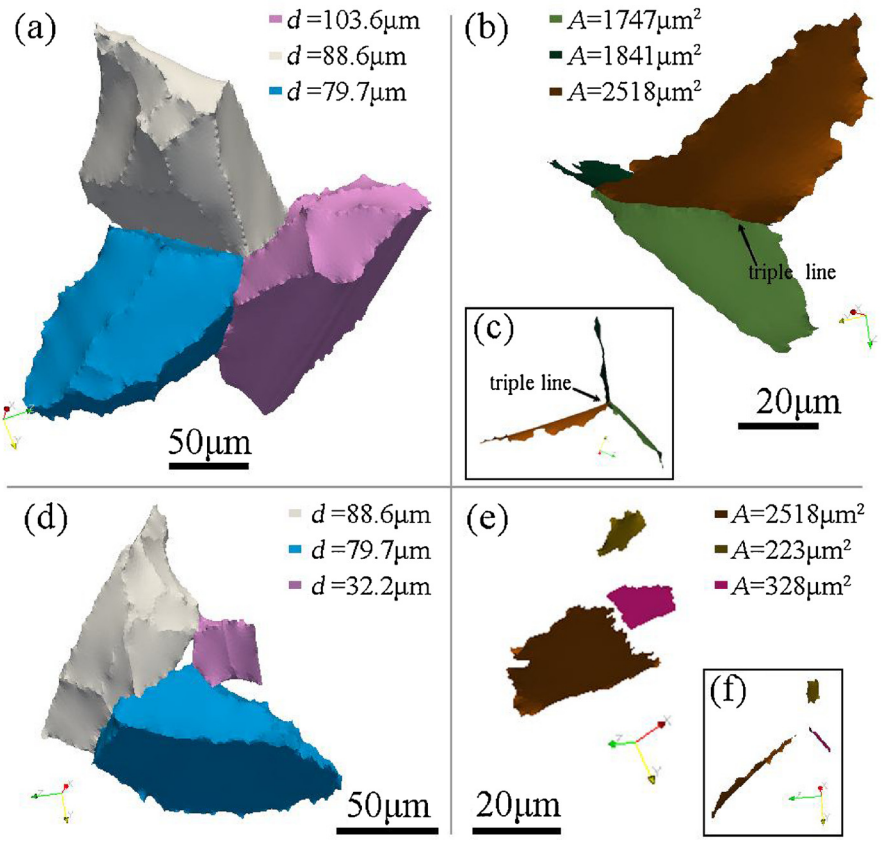

Fig. 5. Examples of three mutually neighboring grains: (a, b, c) the three grains meeting at a triple line and the three boundaries between them; (d, e, f) three grains connected without forming a triple line and the three boundaries between them. 'd' is the grain equivalent spherical diameter and 'A' is the grain boundary area.

the supplemental information. Some in-house Matlab programs were written to quantify the boundary area, grain surface area, and numbers of triple-lines and quadruple-points per grain.

3. Results

Visualizations of the three 3D microstructures are illustrated in Fig. 2. Specimen 316LL (Fig. 2(a–c)) contains 440 grains, which includes 221 completely internal grains and 219 grains that intersect the borders of specimen volume. In specimen 316LS (Fig. 2(d–f)), there are 1540 grains, including 1017 completely internal grains. Specimen 316LGBE (Fig. 2(g–i)) contains 1543 grains, including 905 completely internal grains. A typical grain from 316LL is illustrated in Fig. 3. In the raw data, the grains are composed of voxels as shown in Fig. 3(a). Because real grain boundaries do not have the stair-stepped structures created by the shapes of the voxels, they must be smoothed. In this case, the constrained Laplacian smoothing algorithm in Dream.3D was used and the result is shown in Fig. 3(b). On the left, the grain boundaries are colored according to their misorientations. The color on each face is constant because the misorientation does not change with the GB plane orientation. On the right hand side of Fig. 3(b), the grain boundaries are colored by their orientation, which varies across each grain face because of the GB curvature.

The grain illustrated in Fig. 3 had an equivalent spherical diameter of 127 μm, 31 grains faces, and it was relatively equiaxed. The grain is shown in different projections in Fig. 3(c), so that the shapes of the faces can be seen. Note that the triple lines retain a stair-stepped structure from the original voxels. This is because the triple line positions are constrained in the Laplacian smoothing to prevent significant changes in the GB position. While the grains mostly have equiaxed shapes, more complex grain shapes can also be found. For example, Fig. 4 shows grains with complex shapes including plates, cylinders, tunnels, and highly branched structures. These grains are all twins and illustrate that earlier twin morphology classification schemes developed from 2D observations are incomplete (Mahajan et al., 1997; Meyers and Murr, 1978). Past studies of GB engineered microstructures all focus on CSL boundaries. In this work, attention will be particularly paid to the geometries of the grains and grain boundaries.

3.1. Geometries of three and four grain clusters

In previous studies, triple lines and quadruple points have not received as much attention as grain boundaries (Gertsman, 2001; Hardy and Field, 2016; Shekhar and King, 2008; Zhao et al., 2014). An example of three grains meeting at triple line is illustrated in Fig. 5(a–c). While this is the most common situation for three mutually neighboring grains, it is also possible for three grains to be connected without forming a triple line, as illustrated in Fig. 5(d–f). In this case, the three grains form a ring around a relatively smaller part of another grain. Quadruple points occur where four mutually neighboring grains, four triple lines, and six grain boundaries meet at a point, as illustrated in Fig. 6(a and b). As for the case of three grains in contact, four grains that are connected do not necessarily meet at a point. As illustrated in Fig. 6(c and d), the grains can contact each other in a ring-like structure without sharing a point.

3.2. Grain size distribution

The grain sizes are determined in Dream.3D simply by adding the volumes of all of the voxels within a grain, where the maximum misorientation for voxels within a grain is 15°. With a minimum grain size threshold of 9 voxels, the minimum equivalent grain diameter is 6.5 μm in 316LL and 316LS and is 13.2 μm in 316LGBE. The average grain sizes (equivalent sphere diameters) of the three samples are 41.4 μm

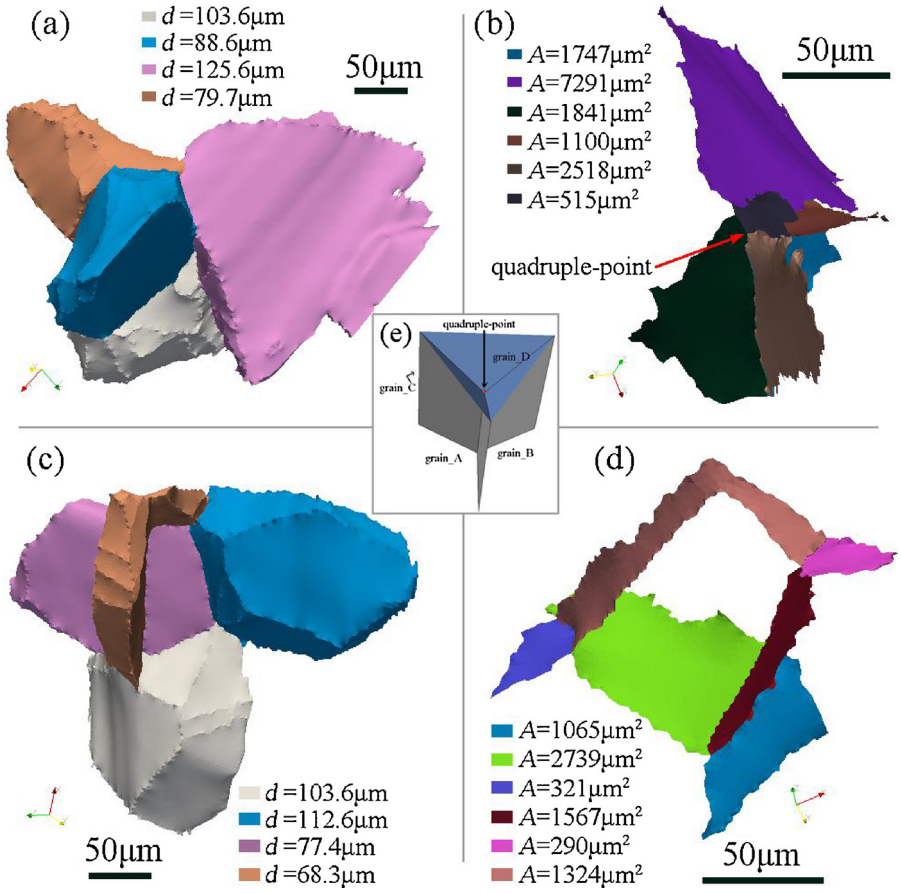

Fig. 6. Examples of four mutually neighboring grains: (a, b) four grains and six grain boundaries meet at a quadruple point; (c, d) four grains connected without forming a quadruple point and the six boundaries between them; (e) schematic of a quadruple point. (Please see the supplementary videos).

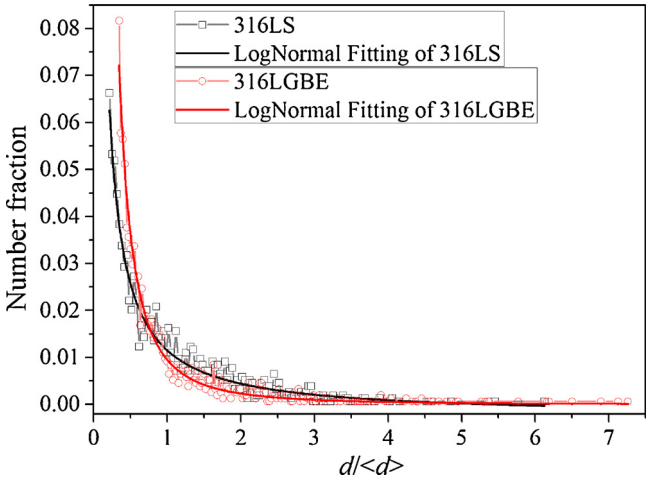

Fig. 7. Grain sizes distributions of grains from the 3D-EBSD microstructures of 316LS and 316LGBE: grain number fractions and their log-normal fitting curves according to Eq. (2). Here the average grain diameter $< d >$ is 30.0 μm for 316LS and 38.3 μm for 316LGBE. The values of w, A, c, and y_0 of log-normal fitting are 6.64 (2.61), 7.03 (66.3), 9.84 (0.045), and −0.00235 (0.00002), respectively, for 316LS (316LGBE).

(316LL), 30.0 μm (316LS) and 38.3 μm (316LGBE). The grain size distributions for 316LS and 316LGBE are illustrated in Fig. 7. Note that throughout the rest of this paper, only 316LS and 316LGBE will be compared, because they have more grains than 316LL and a similar number of grains. The number fraction decreases monotonically with grain diameter for both distributions. In comparison, the GB engineered sample has higher fraction of small grains. In most cases, the distribution of grain sizes (d) is similar to the log-normal distribution (Feltham, 1957; Groeber et al., 2008; Ullah et al., 2014):

$$f(d) = \frac{1}{w\sqrt{2\pi}d} e^{\frac{-[\ln(d/c)]^2}{2w^2}} \quad (1)$$

where w is a constant and c is the median value in the log-normal distribution. The grain sizes in Fig. 7 did not fit well this standard distribution. However, an acceptable fit was obtained by including an additive (y_0) and multiplicative (A) constant, as shown in Eq. (2).

$$y(d) = y_0 + \frac{A}{w\sqrt{2\pi}d} e^{\frac{-[\ln(d/c)]^2}{2w^2}} \quad (2)$$

We also explored the effect of our choices of minimum voxel threshold and minimum misorientation threshold on the grain size distribution. Voxel thresholds of 9, 15, and 20 were chosen, and the misorientation thresholds of 10° and 15° were chosen. The grain size distributions with these choices are shown in Fig. S1 and Fig. S2 (Please see the Supplementary data). All of the distributions have similarly shaped log-normal distributions. Changing the misorientation threshold had no significant influence on the grain size distribution and the average grain size, because there are very few boundaries with misorientations between 2° and 15° (See Fig. S3). The effect of the minimum voxel threshold is mainly on the numbers of small grains, which decrease as the voxel threshold is increased, increasing the apparent average grain size.

3.3. Grain surface area

It is well known that there is an inverse correlation between grain

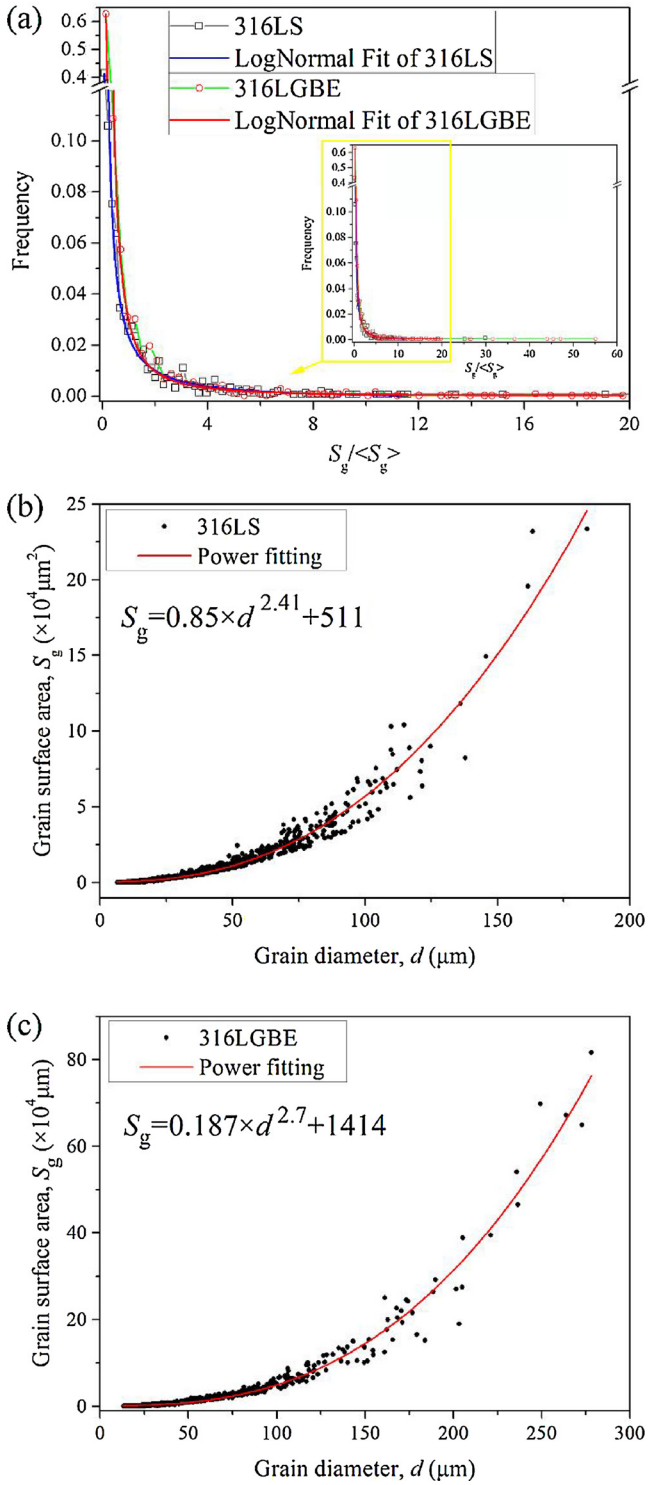

Fig. 8. Surface area statistics of grains from the 3D-EBSD microstructures of 316LS and 316LGBE: (a) distributions of grain surface area and their log-normal fitting curves (Eq. (2)), where the average grain surface areas $< S_g >$ are 7781 μm^2 (316LS) and 14790 μm^2 (316LGBE); (b, c) relationships between the grain surface area and the grain size and their power function fitting curves.

size and strength. The strengthening results from the increase in the grain surface area rather than the grain size itself (Chadwick and Smith, 1976; Meyers and Chawla, 2009). While the grain size and grain surface area are inversely related, the exact dependence is related to grain shape. Because of the twins in the austenitic steels considered here, many grains have non-equiaxed shapes and this makes it difficult to predict the relationship between grain size and surface area. The distributions of grain surfaces areas, fit to the same log-normal distribution used for the grain diameters (Eq. (2)), are shown in Fig. 8(a). Note that there are some grains with very large surface areas that are not described well by the log-normal distribution, and the diameters and areas of the 10 largest grains are tabulated in Table 1. For example, the largest grain in 316LGBE has a diameter of 278 μm and a surface area of 8.2×10^5 μm^2. Note that a spherical grain with the same diameter would have only 30% of this area, indicating that this grain's shape does not compare well to a sphere. As an example, consider the morphology of the fourth largest grain shown in Fig. 4(g). The comparison in Fig. 8 shows that the conventional and GB engineered 316L stainless steel have similar grain surface area distributions.

The relationship between the grain sizes and the grain surface areas of the two samples are shown in Fig. 8(b and c) where they are both fit to a power law. If spheres were good approximations of grain shapes, then the exponents would be exactly two. However, because of the grains' branched and non-equiaxed shapes, the exponent is greater than two. Note that the exponent for the GB engineered sample is larger than that of the conventional sample, suggesting that the grains in the GBE sample have more anisotropic shapes.

The correlations between the surface-to-volume ratio (which we refer to as the specific surface area) and the grain size for the two samples are illustrated in Fig. 9. As expected, the specific surface area decreases with increasing grain size. However, there is a tremendous amount of scatter for the smallest grain sizes and, at the largest grain size, the specific surface area reaches a nearly constant value (the blue lines in Fig. 9). For comparison, the specific surface areas of standard spheres are also illustrated in Fig. 9. Both of the samples have a positive deviation from the ideal spherical shape (more surface area than a sphere) and the GBE sample has a greater deviation.

3.4. Number of faces per grain

It is common to approximate a grain as a polygon with a fixed number of faces, which is equivalent to the number of nearest neighbor grains. While previous work has led to the conclusion that grains have, on average, between 12 and 14 faces, 316LS and 316LGBE have 11.2 and 9.5 faces per grain (Both completely internal grains and border grains were used to calculate the face numbers), respectively. Note that these numbers are influenced by the choices made in the data processing. Specifically, if a 15 voxel grain size threshold is used, then the average for 316LGBE increases to 10.5. The relatively lower average values, when compared to the earlier work, is most likely the result of the extensive twinning. Because twins typically have plate like shapes, they also have fewer than 14 sides and this leads to a lower average. This also explains why the GBE sample has a smaller average number of faces per grain than the reference sample. It should be noted that there are also grains with a large number of sides. For example, the grain that was depicted in Fig. 4(g) has 198 faces, which again is likely to be the result of multiple twinning.

The distributions of the number of faces per grain for the two samples are shown in Fig. 10(a) and fit to the log-normal distribution. The majority of grains (68% in the conventional specimen and 74% in the GB engineered specimen) have fewer than the average number of faces. On the other hand, some grains have more than 100 faces, such as the 10 largest grains that are listed in Table 1. The correlation between the number of faces per grain and the grain size is shown in Fig. 10(b and c). The distributions are fit to a power law. If it is assumed that all grain faces have the same area and grains are spherical, then a quadratic power law is expected. The actual exponent is slightly less than two for both materials. These distributions are similar in shape to those that have been reported previously (Hull, 1988; Kelly et al., 2016; Rowenhorst et al., 2010).

Table 1
Quantities of the 10 largest grains in the 3D-EBSD microstructures of sample 316LS and 316LGBE.

316LS						316LGBE					
Grain ID	Diameter μm	SurfaceArea μm^2	Number of boundaries	Number of TLs	Number of QUs	Grain ID	Diameter μm	SurfaceArea μm^2	Number of boundaries	Number of TLs	Number of QUs
1327	183.8	2.33E5	103	321	448	344	278.1	8.17E5	168	527	872
449	163.3	2.32E5	147	467	728	715	272.8	6.50E5	166	552	910
100	161.5	1.96E5	117	365	553	537	263.7	6.72E5	119	305	357
364	145.7	1.49E5	112	328	535	77	249.3	6.98E5	198	605	1010
578	137.8	8.21E4	41	107	48	254	236.6	4.66E5	91	270	396
193	136.1	1.18E5	77	227	388	778	235.8	5.41E5	142	407	749
1117	124.7	8.98E4	49	143	191	1374	221.1	3.95E5	118	309	413
1510	121.6	6.37E4	48	138	171	325	205.3	3.89E5	92	230	323
302	121.4	8.04E4	57	176	251	1212	205.0	2.75E5	31	81	95
705	120.9	7.32E4	43	119	159	333	203.4	1.90E5	59	155	266

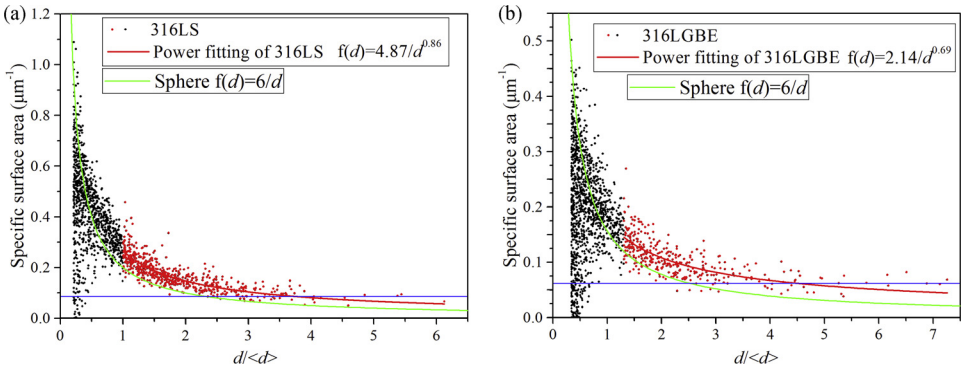

Fig. 9. Correlation between the specific surface area and grain size for the two samples. The data for large grains were colored red and their power law fitting curves were plotted as well. The green lines illustrate the specific surface area of spheres. (For interpretation of the references to colour in this figure legend, the reader is referred to the web version of this article.)

3.5. Grain boundary shape quantities

The distributions of the sizes (equivalent circular diameters) of boundaries (grain faces) are shown in Fig. 11(a). The total number of boundaries in sample 316LS (316LGBE) is 8624 (7053) and the average boundary size is 29.3 μm (42.8 μm). As with the other distributions, the distributions can be fit to a log-normal distribution, but there are many very large faces. For example, sample 316LGBE has a boundary with an equivalent diameter larger than 500 μm. Not surprisingly, there is a positive correlation between grain size and the average diameter of all of the faces on that grain, as shown in Fig. 11(b and c). So, not only do larger grains have more faces, those faces are increasingly larger as the grain size increases.

Applying the approximation that each grain is a polygon, another topological parameter is the edge. Each face is limited by an integer number of edges (these are the triple lines in the microstructure) that can be enumerated. The average numbers of edges per face in the two samples are 4.7 (316LS) and 4.4 (316LGBE). The correlation between the number of edges per grain face and the grain face diameter is shown in Fig. 12. As one might expect, faces with larger diameters have more edges. There is an approximate linear relationship between the number of edges and the face diameter. Because the circumference of a circle is linearly related to the diameter, this relation suggests that the number of edges is linearly related to the perimeter length.

3.6. Triple lines and quadruple points

In sample 316LS and 316LGBE, the average numbers of edges (triple lines) per grain are 26.6 and 21.2, respectively. Note that these are almost exactly equal to half of the average number of faces per grain multiplied by the average number of edges per face (for 316LS, ½·11.2·4.7 = 26.3). The distributions of triple lines per grain are illustrated in Fig. 13(a) and fit to a log-normal distribution. In this case, the fit is not as good as in the previous cases. However, as usual, there are many observations of large grains that have a very large number of triple lines. As shown in Table 1, some grains have more than 200 triple lines. There are also completely enveloped twins that have no triple lines and grains such as the one illustrated in Fig. 4(d) has only one triple line. As illustrated in Fig. 13(b and c), there is a positive correlation between the number of triple lines and the grain diameter and the power law fitting results in an exponent of close to two.

Applying the approximation that each grain is a polygon, the last topological parameter is the vertex or quadruple point where six boundaries and four grains meet at a point in the microstructure. While the nodes shared by six or more boundaries can be quantified automatically using the available software, not all of the nodes are necessarily quadruple points. This is because the 3D microstructure contains some multiple junctions where more than three faces meet at a line. Although these multiple junctions are thought to be an artifact of the resolution and reconstruction of the 3D data rather than a real feature of the microstructure, they create an obstacle to the quantification of quadruple points. Therefore, instead of quadruple points, a new concept of “quadruple union” is proposed here. A quadruple union is an assembly of four mutually neighboring grains that may or may not share a vertex, as shown in Fig. 6. A quadruple union can be a significant microstructure feature. For example, during intergranular stress corrosion cracking, the damage to quadruple unions with three twin-boundaries would be limited by the twin-boundaries whether the four grains share a common point or not.

The quadruple-unions number distribution is shown in Fig. 14(a). Note that, on average, the number of quadruple points per grain should be 2/3 of the number of triple lines per grain, so the average number of quadruple points per grain should be 17.7 for 316LS and 14.1 for 316LGBE. The average numbers of quadruple unions per grain are 32.4

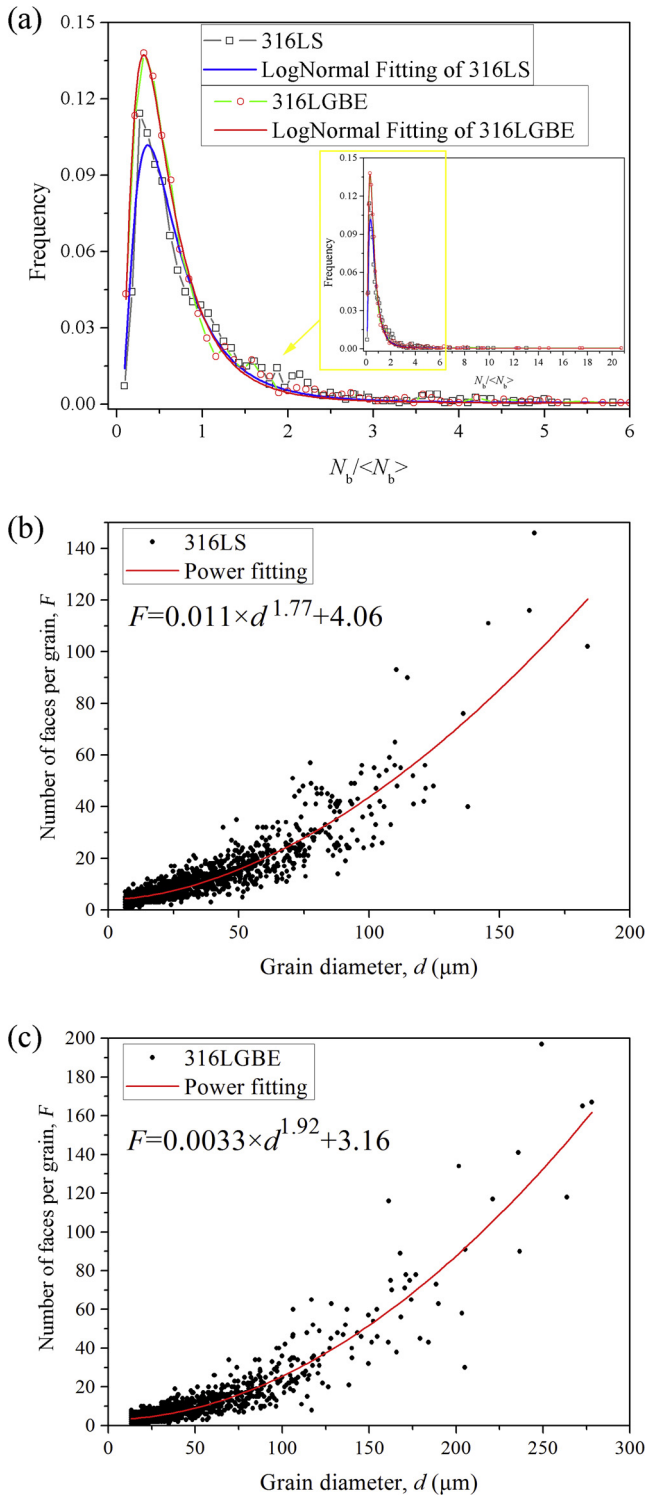

Fig. 10. Statistics of the number of faces (or boundaries) per grain for the 3D-EBSD microstructures of 316LS and 316LGBE: (a) the number distributions of faces per grain and their log-normal fitting curves (Eq. (2)), where the average numbers of faces per grain $< N_b >$ are 11.2 (for 316LS) and 9.5 (for 316LGBE); (b, c) the correlation between the number of faces per grain and the grain size and their power function fitting curves.

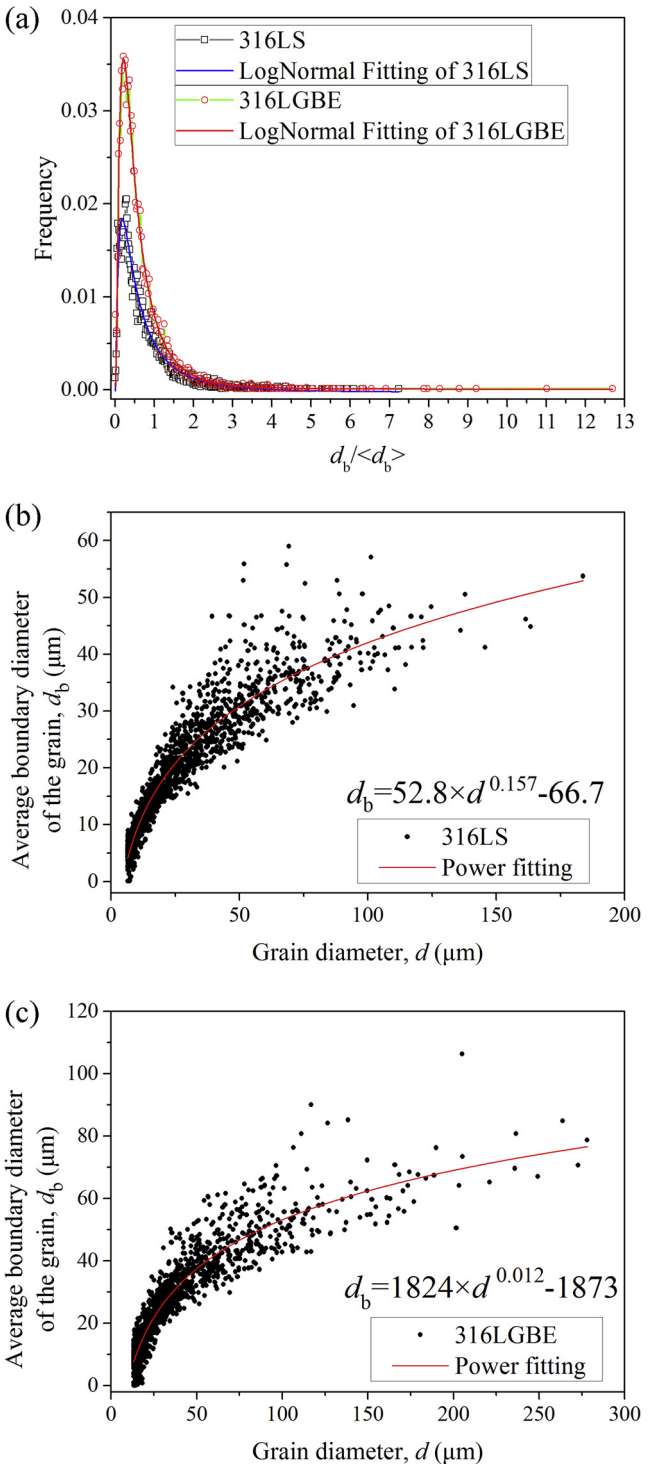

Fig. 11. Statistics of grain boundary areas for the 3D-EBSD microstructures of 316LS and 316LGBE: (a) distributions of the sizes of grain boundaries and their log-normal fitting curves (Eq. (2)), where the average boundary diameters $< d_b >$ are 29.3 μm (316LS) and 42.8 μm (316LGBE); (b, c) the correlation between grain size and the average diameter of all of the faces on that grain and their power function fitting curves.

for 316LS and 27.1 for 316LGBE, which are much larger than the numbers of quadruple points. The quadruple union distribution is similar in many ways to the other distributions. The data for smaller grain sizes can be fit to a log-normal distribution and there are many large values (more than 500 quadruple unions per grain) that are not well described by this distribution, as shown in Table 1. The number of quadruple unions per grains is positively correlated to the grain diameter and the exponent is close to two. This suggests a linear correlation between the number of quadruple points and the surface area of a grain.

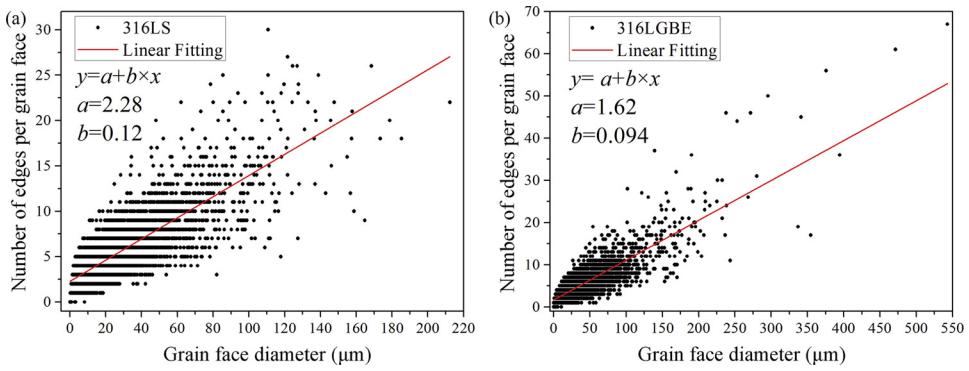

Fig. 12. Correlations between the number of edges per grain face and the face diameter for specimen 316LS and 316LGBE and their linear fitting results.

4. Discussion

4.1. Comparison in grain geometry

In this paper, the geometrical and topological characteristics of grains in an austenitic steel before and after GB engineering are quantitatively compared. The distributions of grain sizes, grain areas, grain faces, and edges are all consistent with a log-normal distribution. Considering the correlations among these parameters, it is not too surprising that they can all be described by the same distribution function. For example, the number of grain faces is strongly correlated to the grain size (See Fig. 10), so it is reasonable that both grain size and the number of grain faces can be described with the same distribution function. The correlations observed here are consistent with findings reported in other recent studies of α-Fe (Ullah et al., 2014; Zhang et al., 2004), a Ni superalloy (Groeber et al., 2008), β-brass (Hull, 1988), and Ti (Kelly et al., 2016; Rowenhorst et al., 2010). In fact, in comparing the available data, it seems apparent that the geometrical shapes of grains in these different materials are more the same than they are different. For example, one of the most commonly reported correlations is between grain size and the numbers of faces, and in each case a very similar power law behavior is observed. Furthermore, the fact that the distributions are consistent with a log-normal distribution goes back to the time of Feltham (Feltham, 1957).

Of course, the main point of this work was to compare the geometrical and topological characteristics of grains in the conventional and GB engineered 316L stainless steel. As with the other metals, most of their characteristics are similar. However, there are two areas in which they differ significantly. The first is in the number of faces per grain (11.2 and 9.5 in the conventional and GB engineered materials on average, respectively). The GB engineered material clearly has fewer faces per grain than the conventional material on average. However, Fig. 10a shows that the maximum face number per grain in the GB engineered material is about 21 times larger than the average number, which is obviously larger than the times (about 13) for the conventional material. This indicates the GB engineered sample has some grains with extremely large number of faces, such as the grain in Fig. 4g. The second area where they differ in the surface area per volume of the grains. As illustrated in Fig. 9, the specific surface area is always greater than the minimum spherical area, but the fitting function has larger deviation from the spherical area function for the GB engineered sample. Additionally, Fig. 9 shows that the largest area per grain is about 55 times larger than the average surface area, which is much larger than the times (about 30) for the conventional material. This implies that, on average, the grain shapes in the GB engineered sample are more eccentric or non-compact shapes than grains in the conventional sample, such as the grain in Fig. 4g.

Both of these observations might be explained by the influence of the GB engineering process on the twin structure. Some twins, such as those illustrated in Fig. 4 (a, d, e and f), have much lower than average numbers of sides and this would reduce the average number of faces per grain. At the same time, the twin can have very non-compact shapes, increasing the specific surface area. Therefore, the differences between the average number of faces per grain and the specific surface area in these two samples are likely connected to the higher number of twins that forms during the GB engineering process. In addition, several grains in the GB engineered material have a huge number of faces and extremely large surface area, such as the grain in Fig. 4g, which are correlated with the multiple twinning process occurs during the GB engineering.

The values for the average number of faces per grain, 11.2 and 9.5 in the conventional and GB engineered materials, are lower than have been found in other metals, for which values between 12 and 14 are most common (Feltham, 1957; Groeber et al., 2008; Hull, 1988; Kelly et al., 2016; Rowenhorst et al., 2010; Ullah et al., 2014; Zhang et al., 2004). There are several possible reasons for this difference. The first might be a result of the parameters used for the reconstruction. We know that the numbers will be larger if we assume a larger minimum grain size. However, this impacts both samples in a similar way so that the GB engineered sample still has fewer faces per grain. It should also be mentioned that among the other materials that have been examined, this is the only one where the result included the effect of twins. Among the other materials, only the Ni superalloy IN100 (Groeber et al., 2008) had a significant amount of twinning and, in that study, the twins were merged with the parent grains. Therefore, the smaller number of faces per grain observed here is due in part to the fact that there were many twins with a smaller number of faces per grain.

4.2. Understanding of GB engineering based on grain geometry

It is well-known that FCC materials after GB engineering have a high proportion of twin-related boundaries (Cao et al., 2017; Liu et al., 2014a,b, 2013; Lind et al., 2016; Michiuchi et al., 2006; Randle, 2004; Xia et al., 2008), large sized grain clusters (Cao et al., 2017; Liu et al., 2013, 2014a,b; Lind et al., 2016; Xia et al., 2008; Xia et al., 2009) and disrupted random boundary network (Kumar et al., 2000; Kobayashi et al., 2016; Michiuchi et al., 2006; Randle, 2004; Telang et al., 2016). These characteristics result in the materials having high resistance to intergranular degradation (Gertsman and Bruemmer, 2001; Hu et al., 2011; Kobayashi et al., 2016; Palumbo et al., 1991; Telang et al., 2016; Tan et al., 2013; Xia et al., 2011; West and Was, 2009). However, how the new findings on the geometrical and topological characteristics of grains, from this work, effect on the philosophy of GB engineering is indeed a significant topic. Firstly, the distributions of grain sizes, grain areas, grain faces, and edges are all consistent with a log-normal distribution in both materials before and after GB engineering. This suggests that the process of GB engineering do not change the entirety of microstructure but the presence of more twin boundaries. In addition, a significant difference between the grain geometrical characteristics of GB engineered and conventional 316L stainless steel is that the GB

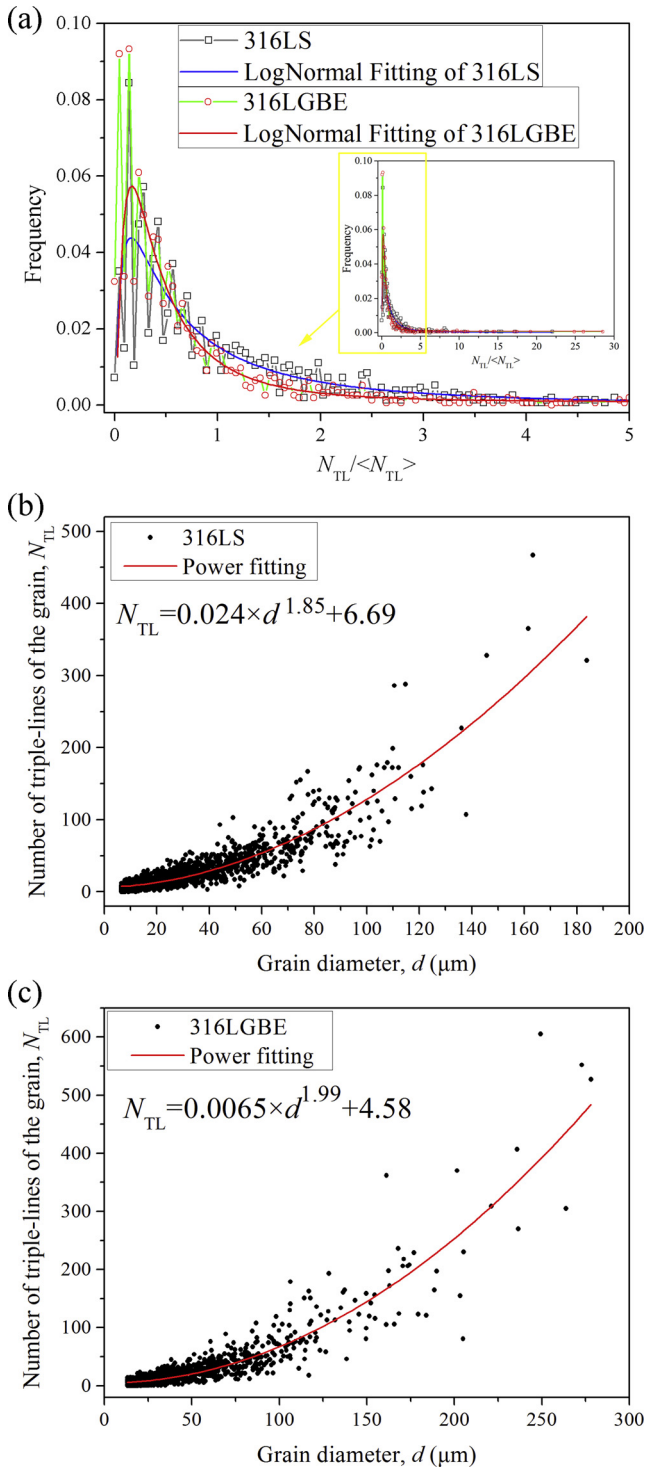

Fig. 13. Statistics of triple lines per grain for the 3D-EBSD microstructures of 316LS and 316LGBE: (a) distributions of the number of triple lines per grain and their log-normal fitting curves (Eq. (2)), where the average numbers of triple lines per grain $< N_{TL} >$ are 26.6 (316LS) and 21.2 (316LGBE); (b, c) the correlations between the number of triple lines per grain and the grain diameter and their power law fitting curves.

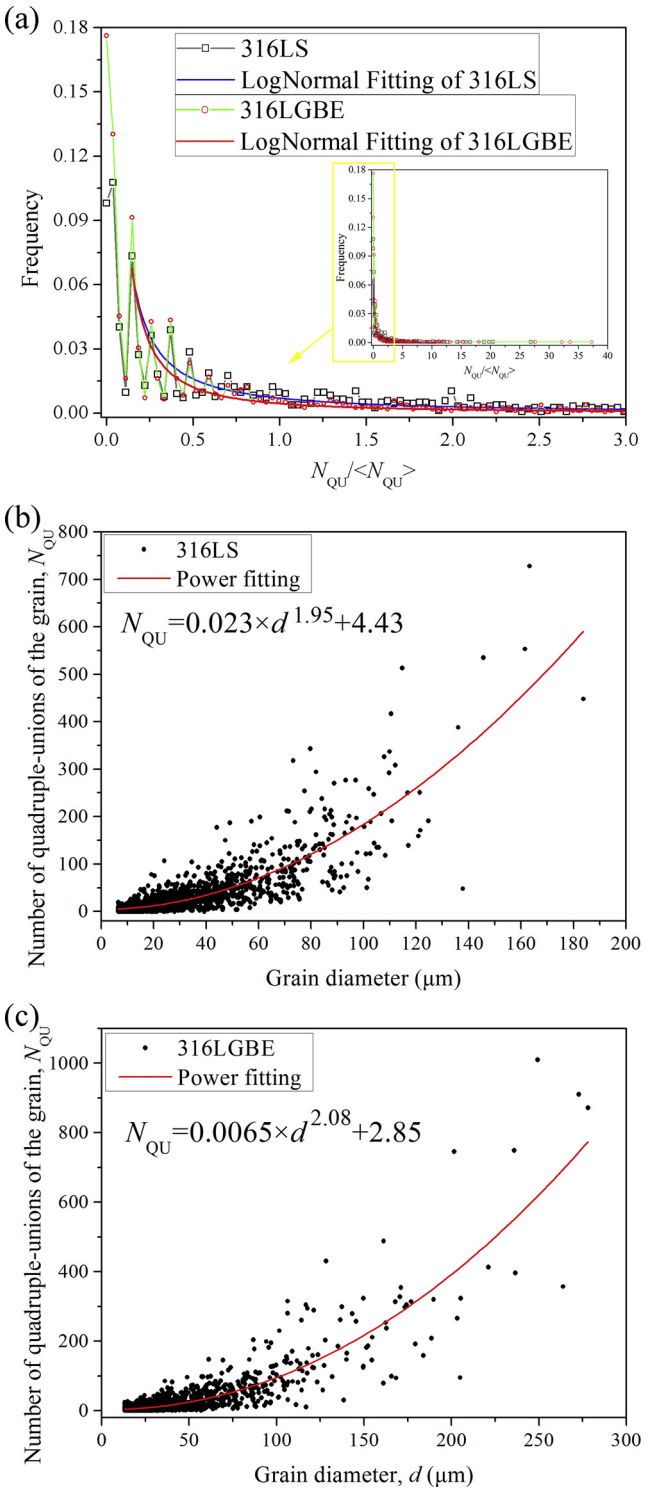

Fig. 14. Statistics of quadruple unions per grain for the 3D-EBSD microstructures of 316LS and 316LGBE: (a) distributions of the number of quadruple unions per grain and their log-normal fitting curves (Eq. (2)), where the average numbers of quadruple unions per grain $< N_{QU} >$ are 32.4 (316LS) and 27.1 (316LGBE); (b, c) the correlations between the number of quadruple unions per grain and the grain diameter and their power law fitting curves.

engineered steel includes some eccentric or non-compact shaped grains with a huge number of faces and extremely high (specific) surface area. These grains would have a positive influence on increasing the resistance to intergranular degradation. The complex morphology of these grains results in extra difficulty or resistance when intergranular degradations propagate along the surfaces of these grains. In other words, the neighboring grains can be bounded together by the eccentric grains to resist intergranular failures.

5. Conclusions

While past studies comparing GB engineered materials with conventional materials found significant differences in the fractions of CSL boundaries, the sizes of twin-related domains, and the random boundary connectivity, the current 3D microstructural study found that the geometrical and topological characteristics of grains in GB engineered and conventional 316L stainless steels are similar in most cases. The distributions of grain sizes, surfaces areas, grain faces, and edges have log-normal distributions in both materials and these quantities are strongly correlated to the grain size. The significant geometric differences between the materials before and after GB engineering are the average number of faces per grain and the surface area per volume of the grains. The grains in the GB engineered steel have fewer faces per grain and more surface area per volume on average. Additionally, there are several eccentric or non-compact shaped grains that have a huge number of faces and extremely large surface area in the GB engineered material. These characteristics are consistent with the introduction of twins during the GB engineering process. These eccentric grains would have a positive influence on increasing the resistance to intergranular degradation.

Acknowledgements

This work was supported by the National Natural Science Foundation of China (NSFC) (grant number 51671122 and 51701017) and Beijing Natural Science Foundation (grant number 2182044). The authors gratefully thank X.T. Zhong (Carnegie Mellon University) for her help with Dream3D and ParaView.

Appendix A. Supplementary data

Supplementary data associated with this article can be found, in the online version, at https://doi.org/10.1016/j.micron.2018.04.002.

References

Alexandreanu, B., Was, G.S., 2006. The role of stress in the efficacy of coincident site lattice boundaries in improving creep and stress corrosion cracking. Scripta Mater. 54, 1047–1052.
Alexandreanu, B., Sencer, B.H., Thaveeprungsriporn, V., Was, G.S., 2003. The effect of grain boundary character distribution on the high temperature deformation behavior of Ni–16Cr–9Fe alloys. Acta Mater. 51, 3831–3848.
Alkemper, J., Voorhees, P.W., 2001. Three-dimensional characterization of dendritic microstructures. Acta Mater. 49, 897–902.
Ayachit, U., 2015. The ParaView Guide: A Parallel Visualization Application. Kitware, NY.
Bhandari, Y., Sarkar, S., Groeber, M., Uchic, M.D., Dimiduk, D.M., Ghosh, S., 2007. 3D polycrystalline microstructure reconstruction from FIB generated serial sections for FE analysis. Comp. Mater. Sci. 41, 222–235.
Brandon, D.G., 1966. The structure of high-angle grain boundaries. Acta Metall. 14, 1479–1484.
Cao, W., Xia, S., Bai, Q., Zhang, W., Zhou, B., Li, Z., Jiang, L., 2017. Effects of initial microstructure on the grain boundary network during grain boundary engineering in Hastelloy N alloy. J. Alloy. Compd. 704, 724–733.
Chadwick, G.A., Smith, D.A., 1976. Grain Boundary Structure and Properties. Academic Press, London.
Feltham, P., 1957. Grain growth in metals. Acta Metall. 5, 97–105.
Gertsman, V.Y., Bruemmer, S.M., 2001. Study of grain boundary character along intergranular stress corrosion crack paths in austenitic alloys. Acta Mater. 49, 1589–1598.
Gertsman, V.Y., 2001. Geometrical theory of triple junctions of CSL boundaries. Acta Crystallogr. A 57, 369–377.
Groeber, M., Jackson, M., 2014. DREAM.3D: a digital representation environment for the analysis of microstructure in 3D. Integr. Mater. Manuf. Innov. 3, 1–17.
Groeber, M., Ghosh, S., Uchic, M.D., Dimiduk, D.M., 2008. A framework for automated analysis and simulation of 3D polycrystalline microstructures: part 1: statistical characterization. Acta Mater. 56, 1257–1273.
Hardy, G.B., Field, D.P., 2016. Reliability of twin-dependent triple junction distributions measured from a section plane. Acta Mater. 103, 809–822.
Hefferan, C.M., Lind, J., Li, S.F., Lienert, U., Rollett, A.D., Suter, R.M., 2012. Observation of recovery and recrystallization in high-purity aluminum measured with forward modeling analysis of high-energy diffraction microscopy. Acta Mater. 60, 4311–4318.
Hu, C.L., Xi, S., Li, H., Liu, T.G., Zhou, B.X., Chen, W.J., Wang, N., 2011. Improving the intergranular corrosion resistance of 304 stainless steel by grain boundary network control. Corros. Sci. 53, 1880–1886.
Hull, F.C., 1988. Plane section and spatial characteristics of equiaxed β-brass grains. Mater. Sci. Technol. 4, 778–785.
Kelly, M.N., Glowinski, K., Nuhfer, N.T., Rohrer, G.S., 2016. The five parameter grain boundary character distribution of α-Ti determined from three-dimensional orientation data. Acta Mater. 111, 22–30.
King, A., Johnson, G., Engelberg, D., Ludwig, W., Marrow, J., 2008. Observations of intergranular stress corrosion cracking in a grain-mapped polycrystal. Science 321, 382–385.
Kobayashi, S., Kobayashi, R., Watanabe, T., 2016. Control of grain boundary connectivity based on fractal analysis for improvement of intergranular corrosion resistance in SUS316L austenitic stainless steel. Acta Mater. 102, 397–405.
Kumar, M., King, W.E., Schwartz, A.J., 2000. Modifications to the microstructural topology in f.c.c. materials through thermomechanical processing. Acta Mater. 48, 2081–2091.
Larson, B.C., Yang, W., Ice, G.E., Budai, J.D., Tischler, J.Z., 2002. Three-dimensional X-ray structural microscopy with submicrometre resolution. Nature 415, 887–890.
Lewis, A.C., Bingert, J.F., Rowenhorst, D.J., Gupta, A., Geltmacher, A.B., Spanos, G., 2006. Two- and three-dimensional microstructural characterization of a super-austenitic stainless steel. Mat. Sci. Eng. A 418, 11–18.
Li, S.F., Mason, J.K., Lind, J., Kumar, M., 2014. Quadruple nodes and grain boundary connectivity in three dimensions. Acta Mater. 64, 220–230.
Lin, F.X., Godfrey, A., Jensen, D.J., Winther, G., 2010. 3D EBSD characterization of deformation structures in commercial purity aluminum. Mater. Charact. 61, 1203–1210.
Lin, B., Jin, Y., Hefferan, C.M., Li, S.F., Lind, J., Suter, R.M., Bernacki, M., Bozzolo, N., Rollett, A.D., Rohrer, G.S., 2015. Observation of annealing twin nucleation at triple lines in nickel during grain growth. Acta Mater. 99, 63–68.
Lind, J., Li, S.F., Kumar, M., 2016. Twin related domains in 3D microstructures of conventionally processed and grain boundary engineered materials. Acta Mater. 114, 43–53.
Liu, T.G., Xia, S., Li, H., Zhou, B.X., Bai, Q., Su, C., Cai, Z.G., 2013. Effect of initial grain sizes on the grain boundary network during grain boundary engineering in Alloy 690. J. Mater. Res. 28, 1165–1176.
Liu, T.G., Xia, S., Li, H., Zhou, B.X., Bai, Q., 2014a. Effect of the pre-existing carbides on the grain boundary network during grain boundary engineering in a nickel based alloy. Mater. Charact. 91, 89–100.
Liu, T.G., Xia, S., Li, H., Zhou, B.X., Bai, Q., 2014b. The highly twinned grain boundary network formation during grain boundary engineering. Mater. Lett. 133, 97–100.
Liu, T., Xia, S., Zhou, B., Bai, Q., Rohrer, G.S., 2017. Three-dimensional characteristics of the grain boundary networks of conventional and grain boundary engineered 316L stainless steel. Mater. Charact. 133, 60–69.
Mahajan, S., Pande, C.S., Imam, M.A., Rath, B.B., 1997. Formation of annealing twins in f.c.c. crystals. Acta Mater. 45, 2633–2638.
Meyers, M.A., Chawla, K.K., 2009. Mechanical Behavior of Materials, 2nd ed. Cambridge University Press, Cambridge.
Meyers, M.A., Murr, L.E., 1978. A model for the formation of annealing twins in F.C.C. metals and alloys. Acta Metall. 26, 951–962.
Michiuchi, M., Kokawa, H., Wang, Z.J., Sato, Y.S., Sakai, K., 2006. Twin-induced grain boundary engineering for 316 austenitic stainless steel. Acta Mater. 54, 5179–5184.
Palumbo, G., King, P.J., Aust, K.T., Erb, U., Lichtenberger, P.C., 1991. Grain boundary design and control for intergranular stress-corrosion resistance. Scripta Metall. Mater. 25, 1775–1780.
Randle, V., 2004. Twinning-related grain boundary engineering. Acta Mater. 52, 4067–4081.
Rohrer, G.S., Miller, H.M., 2010. Topological characteristics of plane sections of polycrystals. Acta Mater. 58, 3805–3814.
Rowenhorst, D.J., Lewis, A.C., Spanos, G., 2010. Three-dimensional analysis of grain topology and interface curvature in a beta-titanium alloy. Acta Mater. 58, 5511–5519.
Saylor, D.M., Morawiec, A., Rohrer, G.S., 2002. Distribution and energies of grain boundaries in magnesia as a function of five degrees of freedom. J. Am. Ceram. Soc. 85, 3081–3083.
Shekhar, S., King, A.H., 2008. Strain fields and energies of grain boundary triple junctions. Acta Mater. 56, 5728–5736.
Spowart, J.E., 2006. Automated serial sectioning for 3-D analysis of microstructures. Scripta Mater. 55, 5–10.
Tan, L., Allen, T.R., Busby, J.T., 2013. Grain boundary engineering for structure materials of nuclear reactors. J. Nucl. Mater. 441, 661–666.
Telang, A., Gill, A.S., Kumar, M., Teysseyre, S., Qian, D., Mannava, S.R., Vasudevan, V.K., 2016. Iterative thermomechanical processing of alloy 600 for improved resistance to corrosion and stress corrosion cracking. Acta Mater. 113, 180–193.
Tokita, S., Kokawa, H., Sato, Y.S., Fujii, H.T., 2017. In situ EBSD observation of grain boundary character distribution evolution during thermomechanical process used for grain boundary engineering of 304 austenitic stainless steel. Mater. Charact. 131, 31–38.
Uchic, M.D., Groeber, M.A., Dimiduk, D.M., Simmons, J.P., 2006. 3D microstructural characterization of nickel superalloys via serial-sectioning using a dual beam FIB-SEM. Scripta Mater. 55, 23–28.
Ullah, A., Liu, G.Q., Luan, J.H., Li, W.W., Rahman, M.U., Ali, M., 2014. Three-dimensional visualization and quantitative characterization of grains in polycrystalline iron. Mater. Charact. 91, 65–75.
Watanabe, T., 1984. Approch to grain boundary design for strong and ductile polycrystals. Res. Mech. 11, 47–84.
Watanabe, T., 2011. Grain boundary engineering: historical perspective and future prospects. J. Mater. Sci. 46, 4095–4115.
West, E.A., Was, G.S., 2009. IGSCC of grain boundary engineered 316L and 690 in

supercritical water. J. Nucl. Mater. 392, 264–271.
Xia, S.A., Zhou, B.X., Chen, W.J., 2008. Effect of single-step strain and annealing on grain boundary character distribution and intergranular corrosion in Alloy 690. J. Mater. Sci. 43, 2990–3000.
Xia, S., Zhou, B.X., Chen, W.J., 2009. Grain cluster microstructure and grain boundary character distribution in alloy 690. Metall. Mater. Trans. A 40a, 3016–3030.
Xia, S., Li, H., Liu, T.G., Zhou, B.X., 2011. Appling grain boundary engineering to Alloy 690 tube for enhancing intergranular corrosion resistance. J. Nucl. Mater. 416, 303–310.
Zhang, C., Suzuki, A., Ishimaru, T., Enomoto, M., 2004. Characterization of three-dimensional grain structure in polycrystalline iron by serial sectioning. Metall. Mater. Trans. A 35, 1927–1933.
Zhao, B., Shvindlerman, L.S., Gottstein, G., 2014. The line tension of grain boundary triple junctions in a Cu-Ni alloy. Mater. Lett. 137, 304–306.